

# Compressed sensing and sparsity in photoacoustic tomography

Markus Haltmeier<sup>1</sup>, Thomas Berer<sup>2</sup>, Sunghwan Moon<sup>3</sup> and Peter Burgholzer<sup>2,4</sup>

<sup>1</sup> Department of Mathematics, University of Innsbruck, Technikerstrasse 13, A-6020 Innsbruck, Austria

<sup>2</sup> Research Center for Non-Destructive Testing (RECENDT), Altenberger Straße 69, 4040 Linz, Austria.

<sup>3</sup> Department of Mathematical Sciences, Ulsan National Institute of Science and Technology, Ulsan 44919, Republic of Korea

<sup>4</sup> Christian Doppler Laboratory for Photoacoustic Imaging and Laser Ultrasonics, Altenberger Straße 69, 4040 Linz, Austria.

E-mail: markus.haltmeier@uibk.ac.at

**Abstract.** Increasing the imaging speed is a central aim in photoacoustic tomography. This issue is especially important in the case of sequential scanning approaches as applied for most existing optical detection schemes. In this work we address this issue using techniques of compressed sensing. We demonstrate, that the number of measurements can significantly be reduced by allowing general linear measurements instead of point-wise pressure values. A main requirement in compressed sensing is the sparsity of the unknowns to be recovered. For that purpose we develop the concept of sparsifying temporal transforms for three-dimensional photoacoustic tomography. We establish a two-stage algorithm that recovers the complete pressure signals in a first step and then applies a standard reconstruction algorithm such as back-projection. This yields a novel reconstruction method with much lower complexity than existing compressed sensing approaches for photoacoustic tomography. Reconstruction results for simulated and for experimental data verify that the proposed compressed sensing scheme allows to significantly reducing the number of spatial measurements without reducing the spatial resolution.

PACS numbers: 43.35.Ud, 87.85.Ng, 43.38.Zp

*Keywords:* Photoacoustic tomography, optoacoustic imaging, compressed sensing, sparsity, non-contact photoacoustic imaging

## 1. Introduction

Photoacoustic tomography (PAT), also known as optoacoustic tomography, is a novel non-invasive imaging technology that beneficially combines the high contrast of pure optical imaging with the high spatial resolution of pure ultrasound imaging (see [1, 2, 3]). The basic principle of PAT is as follows (compare Figure 1). A semitransparent sample (such as a part of a human patient) is illuminated with short pulses of optical radiation. A fraction of the optical energy is absorbed inside the sample which causes thermal heating, expansion, and a subsequent acoustic pressure wave depending on the interior absorbing structure of the sample. The acoustic pressure is measured outside of the sample and used to reconstruct an image of the interior.

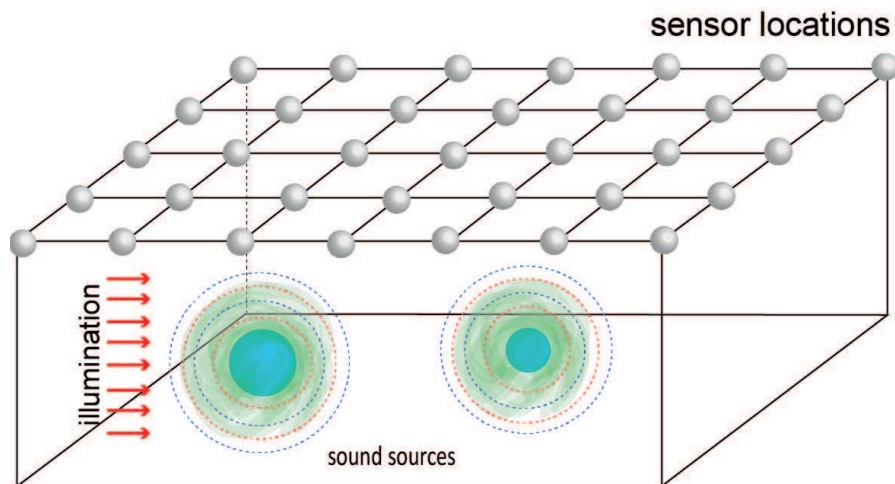


**Figure 1.** BASIC SETUP OF PAT. An object is illuminated with a short optical pulse that induces an acoustic pressure wave. The pressure wave is measured on discrete locations on a surface and used to reconstruct an image of the interior absorbing structure. The small spheres indicate the possible detector or sensor locations on a regular grid on the measurement surface.

### 1.1. Classical measurement approaches

The standard approach in PAT is to measure the acoustic pressure with small detector elements distributed on a surface outside of the sample; see Figure 1. The spatial sampling step size limits the spatial resolution of the pressure data and the (lateral) resolution of the final reconstruction.<sup>‡</sup> Consequently, high spatial resolution requires a large number of detector locations. Ideally, for high frame rate, the pressure data are measured in parallel with a large array made of small detector elements. However, the signal-to-noise ratio and therefore the sensitivity decreases for smaller detector elements and producing a large array with high bandwidth is costly and difficult to fabricate.

<sup>‡</sup> Note that there are several other important factors limiting the resolution of PAT, such as finite detector size, limited detection bandwidth, a limited acoustic aperture, or acoustic attenuation.

As an alternative to the usually employed piezoelectric transducers, optical detection schemes have been used to acquire the pressure data [4, 5, 6, 7]. In these methods an optical beam is raster scanned along a surface. In case of non-contact photoacoustic imaging schemes the ultrasonic waves impinging on the sample surface change the phase of the reflected light, which is demodulated by interferometric means and a photodetector [5, 6, 7]. For Fabry-Perot film sensors, acoustically induced changes of the optical thickness of the sensor lead to a change in the reflectivity, which can be measured using a photo diode [4]. Equally for both techniques, the ultrasonic data are acquired at the location of the interrogation beam by recording the time-varying output of the photodetector. In order to collect sufficient data the measurement process has to be repeated with changed locations of the interrogation beam. Obviously, such an approach slows down the imaging speed. The imaging speed can be increased by multiplying the number of interrogation beams. For example, for a planar Fabry-Perot sensor a detection scheme using 8 interrogation beams has been demonstrated in [8].

Another, less straight forward, approach to increase the measurement speed is the use of patterned interrogation together with compressed sensing techniques. Patterned interrogation was experimentally demonstrated using a digital micromirror device (DMD) in [9, 10]. Using digital micromirror devices or spatial light modulators to generate such interrogation patterns together with compressed sensing techniques allows to reduce the number of spatial measurements without significantly increasing the production costs. For such approaches, we develop a compressed sensing scheme based sparsifying temporal transforms originally introduced for PAT with integrating line detectors in [11, 12].

### 1.2. Compressed sensing

Compressed sensing (or compressive sampling) is a new sensing paradigm introduced recently in [13, 14, 15]. It allows to capture high resolution signals using much less measurements than advised by Shannon's sampling theory. The basic idea in compressed sensing is replacing point measurements by general linear measurements, where each measurement consists of a linear combination

$$\mathbf{y}[j] = \sum_{i=1}^n \mathbf{A}[j, i] \mathbf{x}[i] \quad \text{for } j = 1, \dots, m. \quad (1)$$

Here  $\mathbf{x}$  is the desired high resolution signal (or image),  $\mathbf{y}$  the measurement vector, and  $\mathbf{A}$  the  $m \times n$  measurement matrix. If  $m \ll n$ , then (1) is a severely under-determined system of linear equations for the unknown signal. The theory of compressed sensing predicts that under suitable assumptions the unknown signal can nevertheless be stably recovered from such data. The crucial ingredients of compressed sensing are sparsity and randomness.

- (i) SPARSITY: This refers to the requirement that the unknown signal is sparse, in the sense that it has only a small number of entries that are significantly different from zero (possibly after a change of basis).

- (ii) **RANDOMNESS:** This refers to selecting the entries of the measurement matrix in a certain random fashion. This guarantees that the measurement data are able to sufficiently well separate sparse vectors.

In this work we use randomness and sparsity to develop novel compressed sensing techniques for PAT.

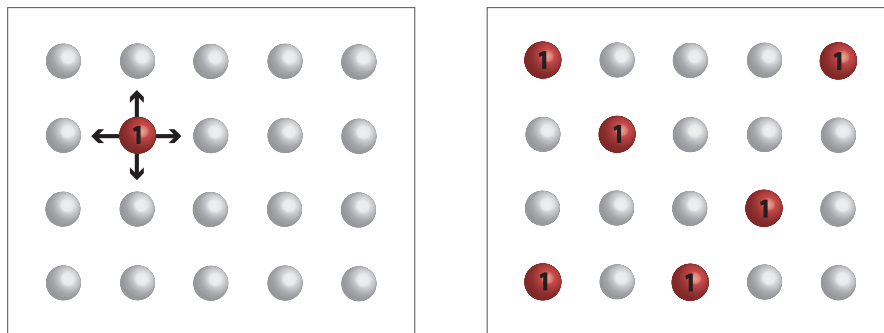


**Figure 2.** STANDARD SAMPLING VERSUS COMPRESSED SENSING. Left: Standard sampling records point-wise data at individual detector positions. Right: Compressed sensing measurements consist of random combinations of point-wise data values.

### 1.3. Compressed sensing in PAT

In PAT, temporal samples can easily be collected at a high rate compared to spatial sampling, where each sample requires a separate sensor. It is therefore natural to work with semi-discrete data  $p(\mathbf{r}_S[i], \cdot)$ , where  $\mathbf{r}_S[i]$  denote locations on the detection surface. Compressed sensing measurements in PAT take the form (1) with  $\mathbf{x}[i] := p(\mathbf{r}_S[i], t)$  for fixed time  $t$ . See Figure 2 for an illustration of classical point-wise sampling versus compressed sensing measurements. In PAT it is most simple to use binary combinations of pressure values, where  $\mathbf{A}[j, i]$  only takes two values (states on and off). Binary measurements can be implemented by optical detection using patterned interrogation and we restrict ourselves to such a situation.

In the PAT literature, two types of binary matrices allowing compressed sensing have been proposed (see Figure 3). In [9, 10] scrambled Hadamard matrices have been used and experimentally realized. In [11, 12] expander matrices have been used, where the measurement matrix is sparse and has exactly  $d$  ones in each column, whose locations are randomly selected. Another possible choice would be a Bernoulli matrix where any entry is selected randomly from two values with equal probability. In all three cases, the random nature of the selected coefficients yields compressed sensing capability of the measurement matrix (see Appendix A for details). As in [11, 12], in this study we use expander matrices. For the experimental verification such measurements are implemented virtually by taking full point-measurements in the experiment and then computing compressed sensing data numerically. This can be seen as proof of principle; implementing pattern interrogation in our contact-free photoacoustic imaging device is an important future aspect.

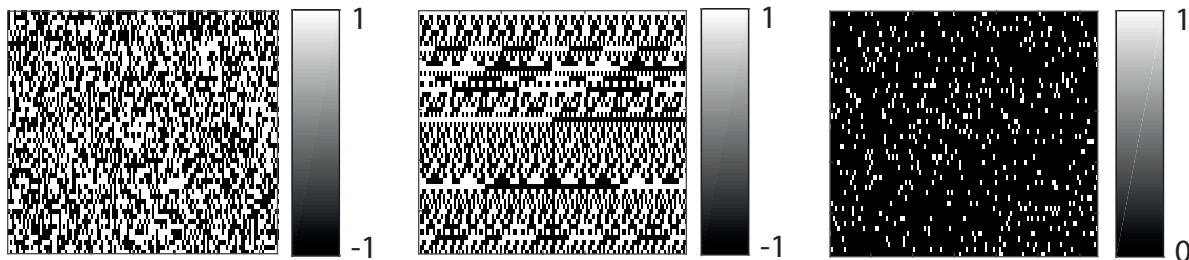


**Figure 3.** BINARY RANDOM MATRICES ALLOWING COMPRESSED SENSING. Left: Bernoulli matrix is dense and unstructured. Center: Subsampled Hadamard matrix is dense and structured. Right: Expander matrix is sparse and unstructured. See Appendix A for more details how to construct these matrices.

Besides the random nature of the measurement matrix, sparsity of the signal to be recovered is the second main ingredient enabling compressed sensing. As in many other applications, sparsity often does not hold in the original domain. Instead sparsity holds in a particular orthonormal basis, such as a wavelet or curvelet basis [16, 17]. However, such a change of basis can destroy the compressed sensing capability of the measurement matrix (for example, in the case of expander matrices). In order to overcome this limitation, in [11, 12] we developed the concept of a sparsifying temporal transformation. Such a transform applies in the temporal variable only and results in a filtered pressure signal that is sparse. Because any operation acting in the temporal domain intertwines with the measurement matrix, one can apply sparse recovery to estimate the sparsified pressure. The photoacoustic source can be recovered, in a second step, by applying a standard reconstruction algorithm to the sparsified pressure.

#### 1.4. Outline of this paper

In this paper we develop a compressed sensing scheme based on a sparsifying transform for three-dimensional PAT (see Section 2). This complements our work [11, 12], where we introduced the concept of sparsifying transforms for PAT with integrating line detectors. Wave propagation is significantly different in two and in three spatial dimensions. As a result, the sparsifying transform proposed in this work significantly differs from the one presented in [11, 12]. In Appendix A we provide an introduction to compressed sensing serving as guideline for designing compressed sensing matrices and highlighting the role of sparsity. In Section 3 we present numerical results on simulated as well as on experimental data from a non-contact photoacoustic imaging setup [18]. These results indicate that the number of spatial measurements can be reduced by at least a factor of 4 compared to the classical point sampling approach. The paper concludes with a discussion presented in Section 4 and a short summary in Section 5.

## 2. Compressed sensing for PAT in planar geometry

In this section we develop a compressed sensing scheme for PAT, where the acoustic signals are recorded on a planar measurement surface. The planar geometry is of particular interest since it is the naturally occurring geometry if using optical detection schemes like the Fabry-Perot sensor or non-contact imaging schemes. We thereby extend the concept of sparsifying temporal transforms introduced for two-dimensional wave propagation in [11, 12]. We emphasize that the proposed sparsifying transform for the three-dimensional wave equation can be used for any detection geometry. An extension of our approach to general geometry would, however, complicate the notation.

### 2.1. PAT in planar geometry

Suppose the photoacoustic source distribution  $p_0(\mathbf{r})$  is located in the upper half space  $\{(x, y, z) \in \mathbb{R}^3 \mid z > 0\}$ . The induced acoustic pressure  $p(\mathbf{r}, t)$  satisfies the wave equation

$$\frac{1}{c^2} \frac{\partial^2 p(\mathbf{r}, t)}{\partial t^2} - \Delta_{\mathbf{r}} p(\mathbf{r}, t) = -\frac{\partial \delta}{\partial t}(t) p_0(\mathbf{r}), \quad (2)$$

where  $\Delta_{\mathbf{r}}$  denotes the spatial Laplacian,  $\partial/\partial t$  is the derivative with respect to time,  $c$  the sound velocity, and  $\delta(t)$  the Dirac delta-function. Here  $(\partial\delta/\partial t)p_0$  acts as the sound source at time  $t = 0$  and it is supposed that  $p(\mathbf{r}, t) = 0$  for  $t < 0$ . We further denote by

$$(\mathcal{W}p_0)(x_S, y_S, t) := p(x_S, y_S, 0, t),$$

the pressure data restricted to the measurement plane. PAT in planar recording geometry is concerned with reconstructing  $p_0$  from measurements of  $\mathcal{W}p_0$ .

For recovering  $p_0$  from continuous data explicit and stable inversion formulas, either in the Fourier domain or in the time domain, are well known. A particularly useful inversion method is the universal backprojection (UBP),

$$p_0(\mathbf{r}) = \frac{z}{\pi} \int_{\mathbb{R}^2} (t^{-1} \partial_t t^{-1} \mathcal{W}p_0)(x_S, y_S, |\mathbf{r} - \mathbf{r}_S|) dS. \quad (3)$$

Here  $\mathbf{r} = (x, y, z)$  is a reconstruction point,  $\mathbf{r}_S = (x_S, y_S, 0)$  a point on the detector surface, and  $|\mathbf{r} - \mathbf{r}_S|$  the distance between  $\mathbf{r}$  and  $\mathbf{r}_S$ . The UBP has been derived in [19] for planar, spherical and cylindrical geometries. The two-dimensional version of the UBP

$$p_0(\mathbf{r}) = -\frac{2z}{\pi} \int_{\mathbb{R}} \int_{|\mathbf{r}-\mathbf{r}_S|}^{\infty} \frac{(\partial_t t^{-1} \mathcal{W}p_0)(x_S, t)}{\sqrt{t^2 - |\mathbf{r} - \mathbf{r}_S|^2}} dt dS,$$

where  $\mathbf{r} = (x, z)$  and  $\mathbf{r}_S = (x_S, 0)$  has been first obtained in [20]. In the recent years, the UBP has been generalized to elliptical observation surface in two and three spatial dimensions [21, 22], and various geometries in arbitrary dimension (see [23, 24, 25]).

## 2.2. Standard sampling approach

In practical application, only a discrete number of spatial measurements can be made. The standard sensing approach in PAT is to distribute detector locations uniformly on a part of the observation surface. Such data can be modeled by

$$\mathbf{p}[i, \cdot] := (\mathcal{W}p_0)(x_S[i], y_S[i], \cdot) \quad \text{for } i = 1, \dots, n. \quad (4)$$

The UBP algorithm applied to semi-discrete data (4) consists in discretizing the spatial integral in (3) using a discrete sum over all detector locations and evaluating it for a discrete number of reconstruction points. This yields to the following UBP reconstruction algorithm.

**Algorithm 1** (UBP algorithm for PAT).

Goal: Recover the source  $p_0$  in (2) from data (4).

(S1) Filtration: For any  $i, t$  compute

$$\mathbf{q}[i, t] \leftarrow \partial_t t^{-1} \partial_t t^{-1} \mathbf{p}[i, t].$$

(S2) Backprojection: For any  $k$  set

$$\mathbf{p}_0[k] \leftarrow v[k]/\pi \sum_{i=1}^{N^3} \mathbf{q}[i, |\mathbf{r}[k] - \mathbf{r}_S[i||] w_i.$$

In Algorithm 1, the first step (S1) can be interpreted as temporal filtering operation. The second step (S2) discretizes the spatial integral in (3) and is called discrete backprojection. The numbers  $w_i$  are weights for the numerical integration and account for density of the detector elements.

## 2.3. Compressed sensing approach

Instead of using point-wise samples, the proposed compressed sensing approach uses linear combinations of pressure values

$$\mathbf{y}[j, \cdot] = \sum_{i=1}^n \mathbf{A}[j, i] \mathbf{p}[i, \cdot] \quad \text{for } j \in \{1, \dots, m\}, \quad (5)$$

where  $\mathbf{A}$  is a binary  $m \times n$  random matrix, and  $\mathbf{p}[i, t]$  are point-wise pressure data. In the case of compressed sensing we have  $m \ll n$ , which means that the number of measurements is much smaller than the number of point-samples. As shown in Appendix A, Bernoulli matrices, subsampled Hadamard matrices as well as expander matrices are possible compressed sensing matrices.

In order to recover the photoacoustic source from compressed sensing data (5), one can use the following two-stage procedure. In the first step we recover the point-wise pressure values from the compressed sensing measurements. In the second step, one applies a standard reconstruction procedure (such as the UBP Algorithm 1) to the estimated point-wise pressure to obtain the photoacoustic source. The first step can

be implemented by setting  $\hat{\mathbf{p}}[\cdot, t] := \mathbf{\Psi}\hat{\mathbf{x}}[\cdot, t]$ , where  $\hat{\mathbf{x}}[\cdot, t]$  minimizes the  $\ell^1$ -Tikhonov functional

$$\frac{1}{2}\|\mathbf{y}[\cdot, t] - \mathbf{A}\mathbf{\Psi}\hat{\mathbf{x}}\|^2 + \lambda\|\hat{\mathbf{x}}\|_1 \rightarrow \min_{\hat{\mathbf{x}}} . \quad (6)$$

Here  $\mathbf{\Psi} \in \mathbb{R}^{n \times n}$  is a suitable basis (such as orthonormal wavelets) that sparsely represents the pressure data and  $\lambda$  is a regularization parameter. Note that (6) can be solved separately for every  $t \in [0, T]$  which makes the two-stage approach particularly efficient. The resulting two-stage reconstruction scheme is summarized in Algorithm 2.

**Algorithm 2** (Two-stage compressed sensing reconstruction scheme).

Goal: Recover  $p_0$  from data (5).

(S1) Recovery of point-measurements:

- ◆ Choose a sparsifying basis  $\mathbf{\Psi} \in \mathbb{R}^{n \times n}$ .
- ◆ For every  $t$ , find an approximation  $\hat{\mathbf{p}}[\cdot, t] := \mathbf{\Psi}\hat{\mathbf{x}}[\cdot, t]$  by minimizing (6).

(S2) Recover  $p_0$  by applying a PAT standard reconstruction algorithm to  $\hat{\mathbf{p}}[\cdot, t]$ .

As an alternative to the proposed two-stage procedure, the photoacoustic source could be recovered directly from data (5) based on minimizing the  $\ell^1$ -Tikhonov regularization functional [26, 27]

$$\frac{1}{2}\|\mathbf{y} - (\mathbf{A} \circ \mathcal{W})\hat{p}_0\|_2^2 + \lambda\|\mathbf{\Psi}\hat{p}_0\|_1 \rightarrow \min_{\hat{p}_0} . \quad (7)$$

Here  $\mathbf{\Psi}$  is a suitable basis that sparsifies the photoacoustic source  $p_0$ . However, such an approach is numerically expensive since the three-dimensional wave equation and its adjoint have to be solved repeatedly. The proposed two-step reconstruction scheme is much faster because it avoids evaluating the wave equation, and the iterative reconstruction decouples into lower-dimensional problems for every  $t$ . A simple estimation of the number of floating point operations (flops) reveals the dramatic speed improvement. Suppose we have  $n = N \times N$  detector locations,  $\mathcal{O}(N)$  time instance and recover the source on an  $N \times N \times N$  spatial grid. Evaluation of a straight forward time domain discretization of  $\mathcal{W}$  and its adjoint require  $\mathcal{O}(N^5)$  flops. Hence, the iterative one-step reconstruction requires  $N_{\text{iter}}\mathcal{O}(N^5)$  operations, where  $N_{\text{iter}}$  is the number of iterations. On the other hand the two-stage reconstruction requires  $N_{\text{iter}}\mathcal{O}(N^3m)$  flops for the iterative data completion and additionally  $\mathcal{O}(N^5)$  flops for the subsequent UBP reconstruction. In the implementation one takes the number of iterations (at least) in the order of  $N$  and therefore the two-step procedure is faster by at least one order of magnitude.

Compressed sensing schemes without using random measurements have been considered in [28, 29, 30]. In these approaches an optimization problem of the form (7) is solved, where  $\mathbf{A}$  is an under-sampled measurement matrix. Especially when combined with a total variation penalty such approaches yields visually appealing result.



Strictly taken, the measurements used there are not shown to yield compressed sensing, which would require some form of incoherence between the measurement matrix and the sparsifying basis (usually established by randomness). For which class of phantoms undersampled point-wise measurements have compressed sensing capability for PAT is currently an unsolved problem.

#### 2.4. Sparsifying temporal transform

In order that the pressure data can be recovered by (6) one requires a suitable basis  $\Psi \in \mathbb{R}^{n \times n}$  such that the pressure is sparsely represented in this basis and that the composition  $\mathbf{A} \circ \Psi$  is a proper compressed sensing matrix. For expander matrices these two conditions are not compatible. To overcome this obstacle in [11, 12] we developed the concept of a sparsifying temporal transform for the two-dimensional case in circular geometry. Below we extend this concept to three spatial dimensions using combinations of point-wise pressure values.

Suppose we apply a transformation  $\mathbf{T}$  to the data  $t \mapsto \mathbf{y}[\cdot, t]$  that only acts in the temporal variable. Because the measurement matrix  $\mathbf{A}$  is applied in the spatial variable, the transformation  $\mathbf{T}$  and the measurement matrix commute, which yields

$$\mathbf{T}\mathbf{y} = \mathbf{A}(\mathbf{T}\mathbf{p}). \quad (8)$$

We call  $\mathbf{T}$  a sparsifying temporal transform, if  $\mathbf{T}\mathbf{p}[\cdot, t] \in \mathbb{R}^n$  is sufficiently sparse for a suitable class of source distributions and all times  $t$ . In this work we propose the following sparsifying spatial transform

$$\mathbf{T}(\mathbf{p}) := t^3 \partial_t t^{-1} \partial_t t^{-1} \mathbf{p}. \quad (9)$$

The sparsifying effect of this transform is illustrated in Figure 4 applied to the pressure data arising from a uniform spherical source. The reason for choice of (9) is as follows: It is well known that the pressure signals induced by a uniform absorbing sphere has an N-shaped profile. Therefore, applying the second temporal derivative to  $\mathbf{p}$  yields a signal that is sparse. The modification of the second derivative is used because the term  $\partial_t t^{-1} \mathbf{p}$  appears in the universal backprojection and therefore only one numerical integration is required in the implementation of our approach. Finally, we empirically found that the leading factor  $t^3$  results in well balanced peaks in Figure 4 and yields good numerical results.

Having a sparsifying temporal transform at hand, we can construct the photoacoustic source by the following modified two-stage approach. In the first step recover an approximation  $\hat{\mathbf{q}}[\cdot, t] \simeq \mathbf{T}\mathbf{p}[\cdot, t]$  by solving

$$\frac{1}{2} \|\mathbf{T}\mathbf{y}[\cdot, t] - \mathbf{A}\hat{\mathbf{q}}[\cdot, t]\|^2 + \lambda \|\hat{\mathbf{q}}[\cdot, t]\|_1 \rightarrow \min_{\hat{\mathbf{q}}} . \quad (10)$$

In the second step, we recover the photoacoustic source by implementing the UBP expressed in terms of the sparsified pressure,

$$p_0(\mathbf{r}) = -\frac{z}{\pi} \int_{\mathbb{R}^2} \int_{|\mathbf{r}-\mathbf{r}_S|}^{\infty} (t^{-3} \mathbf{T}\mathcal{W}p_0)(x_S, y_S, t) dt dS. \quad (11)$$

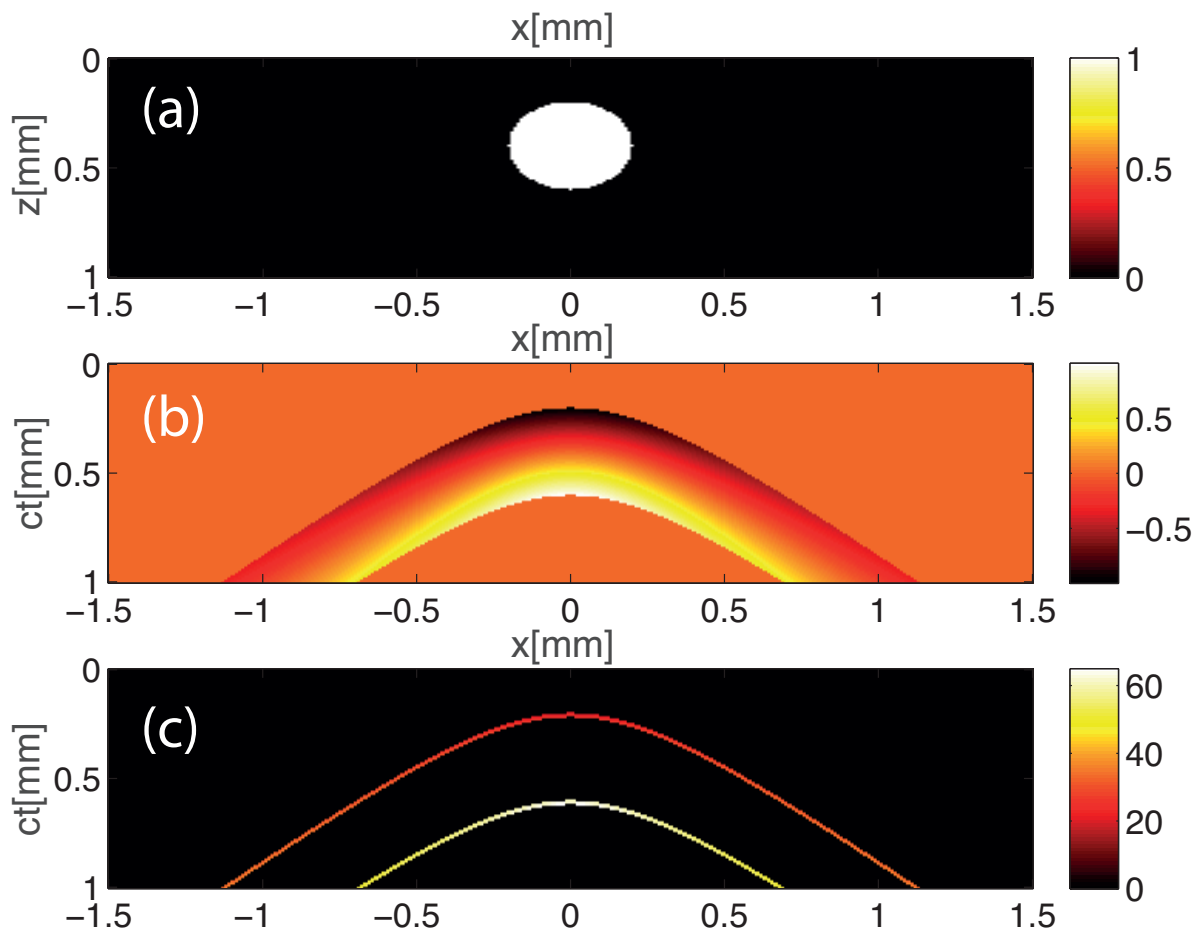


**Figure 4.** EFFECT OF THE SPARSIFYING TRANSFORM. Top: Cross section of a uniform spherical source. Middle: Corresponding pressure data. Bottom: Result after applying the sparsifying transform  $\mathbf{T}$ .

Here  $\mathbf{r} = (x, y, z)$  is a reconstruction point and  $\mathbf{r}_S = (x_S, y_S, 0)$  a point on the measurement surface. The modified UBP formula (11) can be implemented analogously to Algorithm 1. In summary, we obtain the following reconstruction algorithm.

**Algorithm 3** (Compressed sensing reconstruction with sparsifying temporal transform).

Goal: Reconstruct  $p_0$  in (2) from data (5).

(S1) Recover sparsified point-measurements:

- ◆ Compute the filtered data  $\mathbf{T}\mathbf{y}(t)$
- ◆ Recover an approximation  $\hat{\mathbf{q}}[\cdot, t]$  to  $\mathbf{T}\mathbf{p}[\cdot, t]$  by solving (10).

(S2) UBP algorithm for sparsified data:

- ◆ For any  $i, \rho$  set  $\mathbf{q}[i, \rho] \leftarrow \int_{\rho}^{\infty} t^{-3} \mathbf{q}[i, t] dt$

◆ For any  $k$  set

$$p_0^{\text{CS}}[k] \leftarrow \frac{v[k]}{\pi} \sum_{i=1}^N \mathbf{q}[i, |\mathbf{r}[k] - \mathbf{r}_S[i||] w_i.$$

Since (10) can be solved separately for every  $t$ , the modified two-stage Algorithm 3 is again much faster than a direct approach based on (7). Moreover, from general recovery results in compressed sensing presented in the Appendix, 3 yields theoretical recovery guarantees for Bernoulli, subsampled Hadamard matrices as well as expander matrices (adjacency matrices of left  $d$ -regular graphs); see Figure 3.

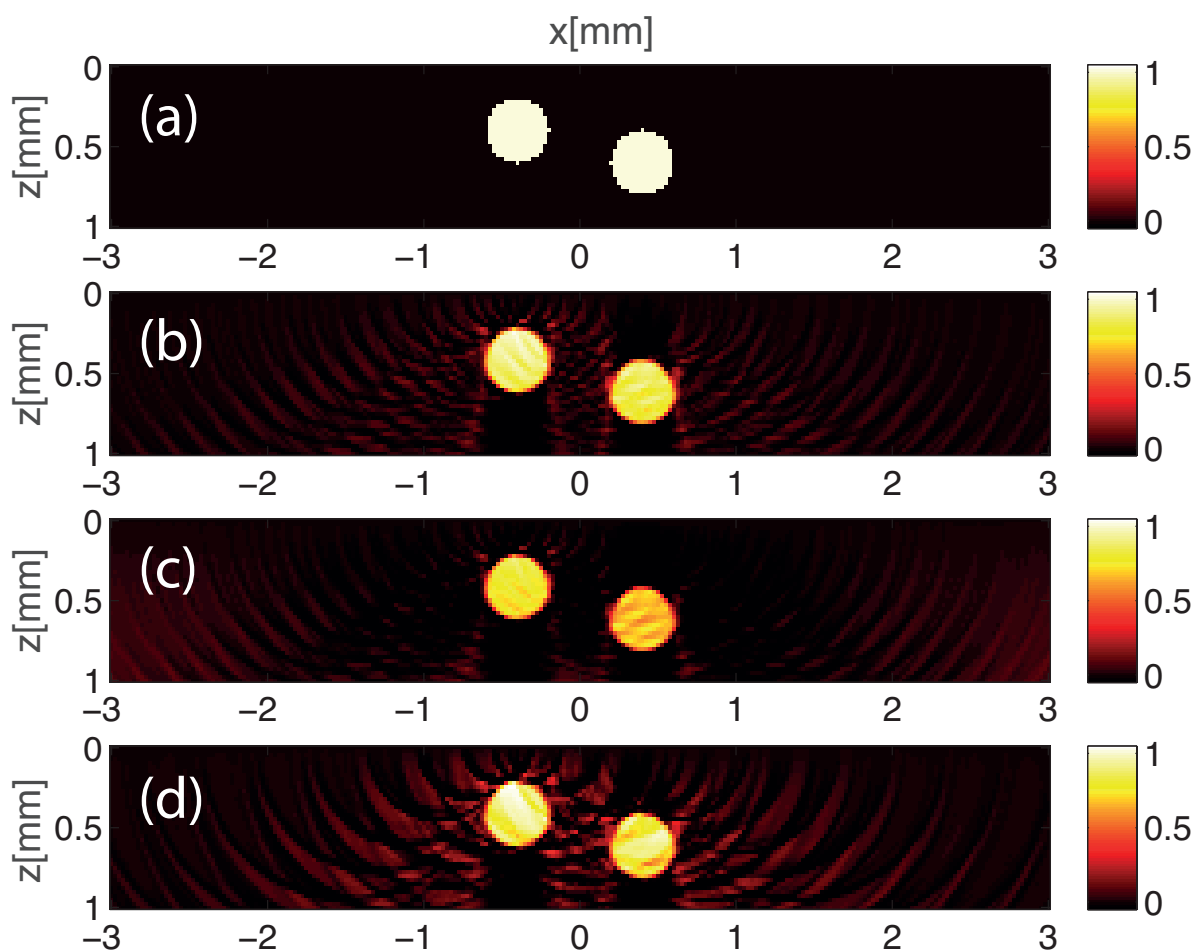


**Figure 5.** THREE-DIMENSIONAL COMPRESSED SENSING PAT VERSUS STANDARD APPROACH. (a) Cross section of superposition of two uniform spherical absorbers. (b) Reconstruction using 4096 point measurements on a Cartesian grid. (c) Compressed sensing reconstruction using 1024 measurements with  $d = 15$ . (d) Reconstruction using 1024 point measurements on a Cartesian grid.

	4096 standard	1024 standard	1024 CS
$\alpha = 1$	0.0472	0.0660	0.0409
$\alpha = 2$	0.1046	0.1256	0.1124

**Table 1.** Normalized  $\ell^\alpha$ -reconstruction errors for  $\alpha = 1, 2$ .

### 3. Numerical and experimental results

#### 3.1. Results for simulated data

We consider reconstructing a superposition of two spherical absorbers, having centers in the vertical plane  $\{(x, y, z) \in \mathbb{R}^3 \mid y = 0\}$ . The vertical cross section of the photoacoustic source is shown in Figure 5(a). In order to test our compressed sensing approach we first create point samples of the pressure  $\mathcal{W}p_0$  on an equidistant Cartesian grid on the square  $[-3, 3] \times [-3, 3]$  using  $64 \times 64$  grid points. From that we compute compressed sensing data

$$\mathbf{y}[j, t] = \sum_{i=1}^{4096} \mathbf{A}[j, i] \mathbf{p}[i, t] \quad \text{for } j \in \{1, \dots, 1024\}. \quad (12)$$

The choice  $m = 1024$  corresponds to an reduction of measurements by a factor 4. The expander matrix  $\mathbf{A}$  was chosen as the adjacency matrix of a randomly left  $d$ -regular graph with  $d = 15$ ; see Example 10 in the Appendix. The pressure signals  $\mathbf{p}[i, t]$  have been computed by the explicit formula for the pressure of a uniformly absorbing sphere [31] and evaluated at 243 times points  $ct$  uniformly distributed in the interval  $[0, 6]$ .

Figure 5 shows the reconstruction results using 4096 point samples using Algorithm 1 (Figure 5(b)) and the reconstruction from 1024 compressed sensing measurements using Algorithm 3 (Figure 5(c)). The reconstruction has been computed at  $241 \times 41$  grid points in a vertical slice of size  $[-3, 3] \times [0, 1]$ . The  $\ell^1$ -minimization problem (10) has been solved using the FISTA [32]. For that purpose the matrix  $\mathbf{A}$  has been rescaled to have 2-norm equal to one. The regularization parameter has then been set to  $\lambda = 10^{-5}$  and we applied 7500 iterations of the FISTA with maximal step size equal to one. We see that the image quality from the compressed sensing reconstruction is comparable to the reconstruction from full data using only a fourth of the number of measurements. For comparison purpose, Figure 5(d) also shows the reconstruction using 1024 point samples. One clearly recognizes the increase of undersampling artifacts and worse image quality compared to the compressed sensing reconstruction using the same number of measurements. A more precise error evaluation is given in Table 1, where we show the normalized  $\ell^\alpha$ -error  $\sqrt[\alpha]{\sum_k |p_0[k] - p_0^{\text{CS}}[k]|^\alpha / N}$  for  $\alpha = 1$  and  $\alpha = 2$ . The reconstruction error in  $\ell^1$ -norm is even slightly smaller for the compressed sensing reconstruction than for the full reconstruction. This might be due to a slight denoising effect of  $\ell^1$ -minimization that removes some small amplitude errors (contributing more to the more  $\ell^1$ -norm than to the  $\ell^2$ -norm). Figure 6 shows the pressure corresponding to the

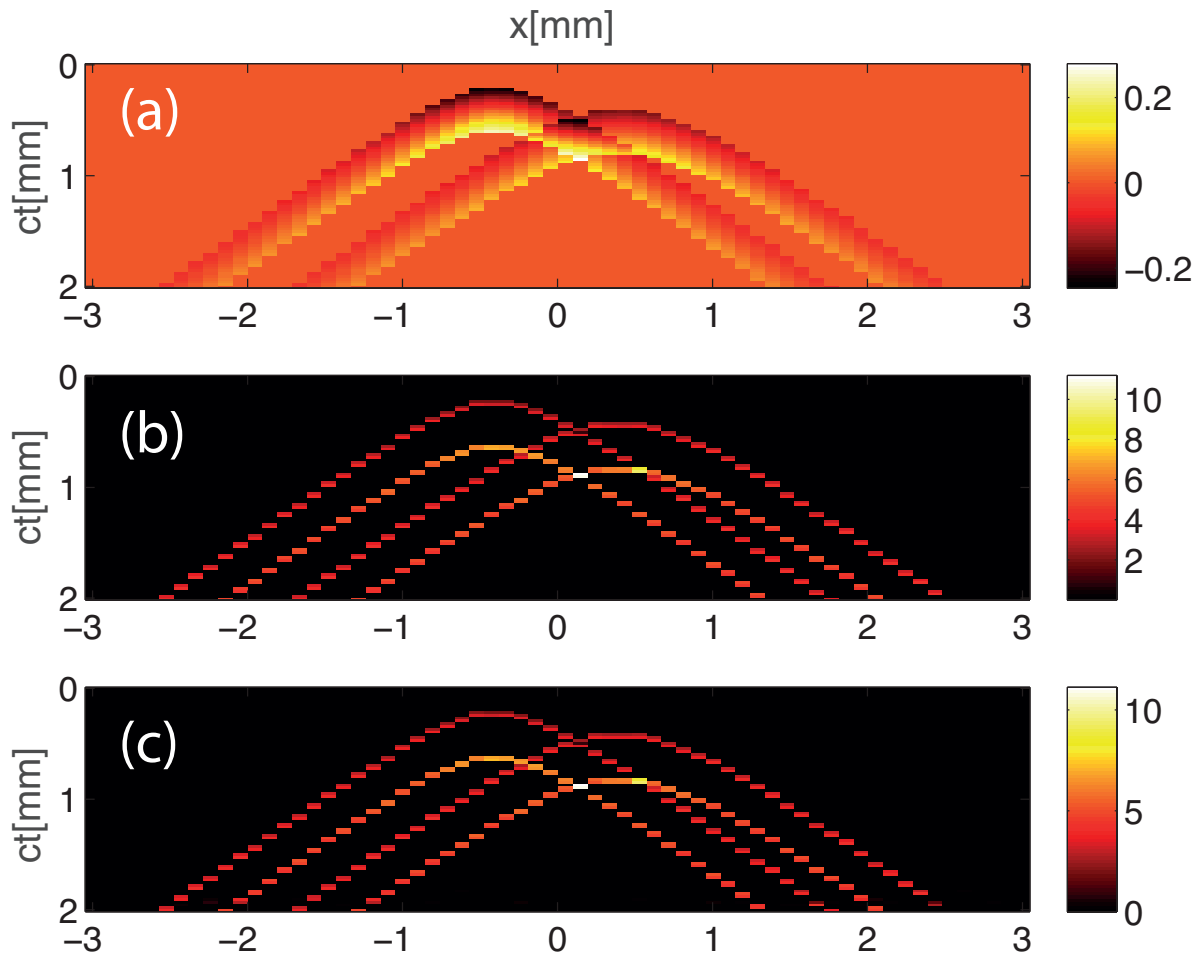


**Figure 6.** RESULT OF SPARSE RECOVERY. (a) Pressure at  $z = 0$  induced by two spherical absorbers shown in Figure 5. (b) Result after applying the sparsifying transform. (c) Reconstruction of the sparsified pressure from compressed sensing measurements using  $\ell^1$  minimization.

absorbers shown in Figure 5 together with the sparsified pressure and its reconstruction from compressed sensing data.

Finally, Figure 7 shows the reconstruction (restricted to  $[-1, 1] \times [0, 1]$ ) using Algorithm 3 for varying compression factors  $n/m = 16, 8, 4, 2, 1$ . In all cases  $d = 15$  and  $\lambda = 10^{-5}$  have been used and 7500 iterations of the FISTA have been applied. As expected, the reconstruction error increases with increasing compression factor. One further observes that the compression factor of 4 seems a good choice since for smaller compression factor the error increases more severely. In our numerical studies (not shown) we observed that also for different discretizations a compression factor of 4 is a good choice.

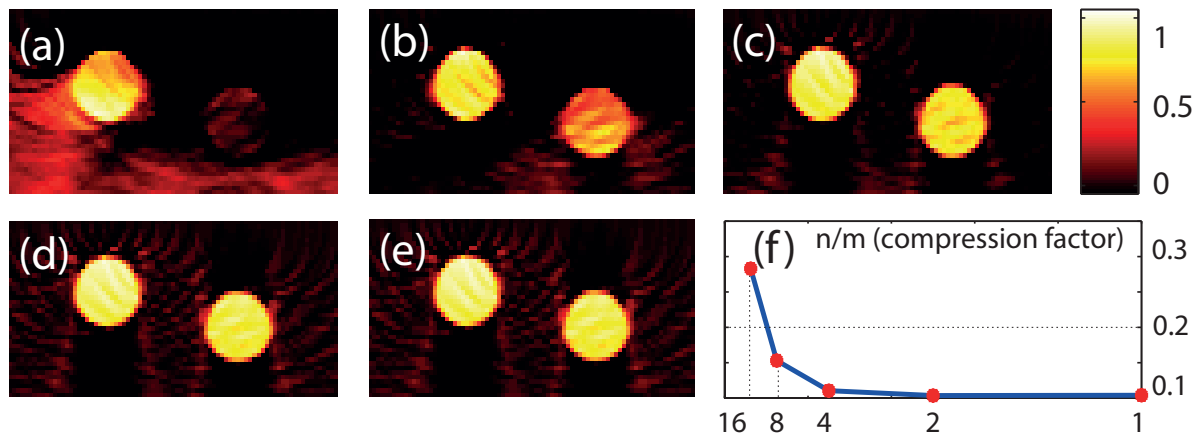


**Figure 7.** RECOVERY RESULTS FOR VARYING COMPRESSION FACTOR  $n/m$ . (a)  $n/m = 16$ . (b)  $n/m = 8$ . (c)  $n/m = 4$ . (d)  $n/m = 2$ . (e)  $n/m = 1$ . (f) Normalized  $\ell^2$ -reconstruction in dependence of the compression factor.

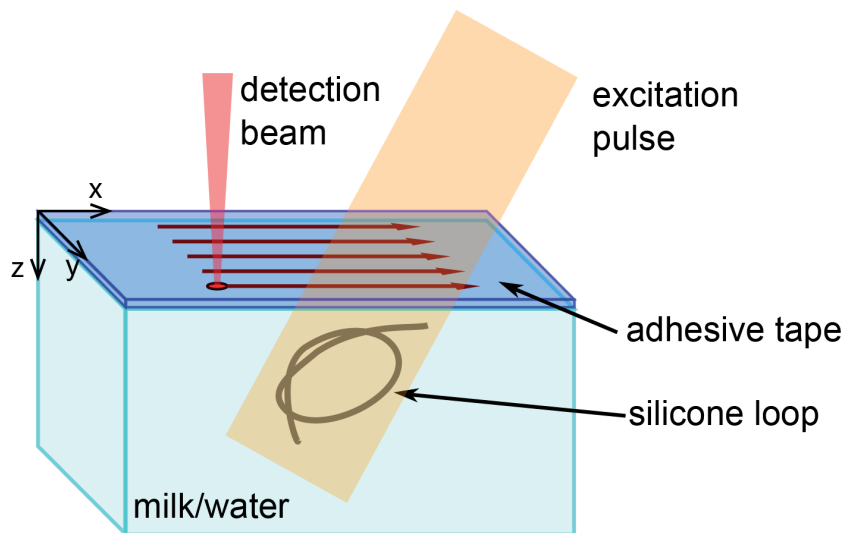


**Figure 8.** SCHEMATIC OF EXPERIMENTAL SETUP OF NON-CONTACT PHOTOACOUSTIC IMAGING. Photoacoustic waves are excited by short laser pulses. The ultrasonic signals are measured on the surface of the sample using a non-contact photoacoustic imaging technique.

### 3.2. Results for experimental data

Experimental data have been obtained from a silicone tube phantom as shown in Figure 8. The silicone tube was filled with black ink (Pelikan 4001 brilliant black, absorption coefficient of  $54/\text{cm}$  at  $740\text{ nm}$ ), formed to a knot, and immersed in a milk/water emulsion. The outer and inner diameters of the tube were  $600\ \mu\text{m}$  and  $300\ \mu\text{m}$ , respectively. Milk was diluted into the water to mimic the optical scattering properties of tissue; an adhesive tape, placed on the top of the water/milk emulsion, was used to mimic skin. Photoacoustic signals were excited at a wavelength of  $740\text{ nm}$  with nanosecond pulses from an optical parametric oscillator pumped by a frequency

doubled Nd:YAG laser. The radiant expose was  $105 \text{ Jm}^{-2}$ , which is below the maximum permissible exposure for skin of  $220 \text{ Jm}^{-2}$ . The resulting ultrasonic signals were detected on the adhesive tape by a non-contact photoacoustic imaging setup as described in [18]. In brief, a continuous wave detection beam with a wavelength of  $1550 \text{ nm}$  was focused onto the sample surface. The diameter of the focal spot was about  $12 \mu\text{m}$ . Displacements on the sample surface, generated by the impinging ultrasonic waves, change the phase of the reflected laser beam. By collecting and demodulating the reflected light, the phase information and, thus, information on the ultrasonic displacements at the position of the laser beam can be obtained. To allow three-dimensional measurements, the detection beam is raster scanned along the surface. The obtained displacement data do not fulfill the wave equation and cannot be used for image reconstruction directly. Thus, to convert the displacement data to a quantity (roughly) proportional to the pressure, the first derivative in time of the data was calculated [5].

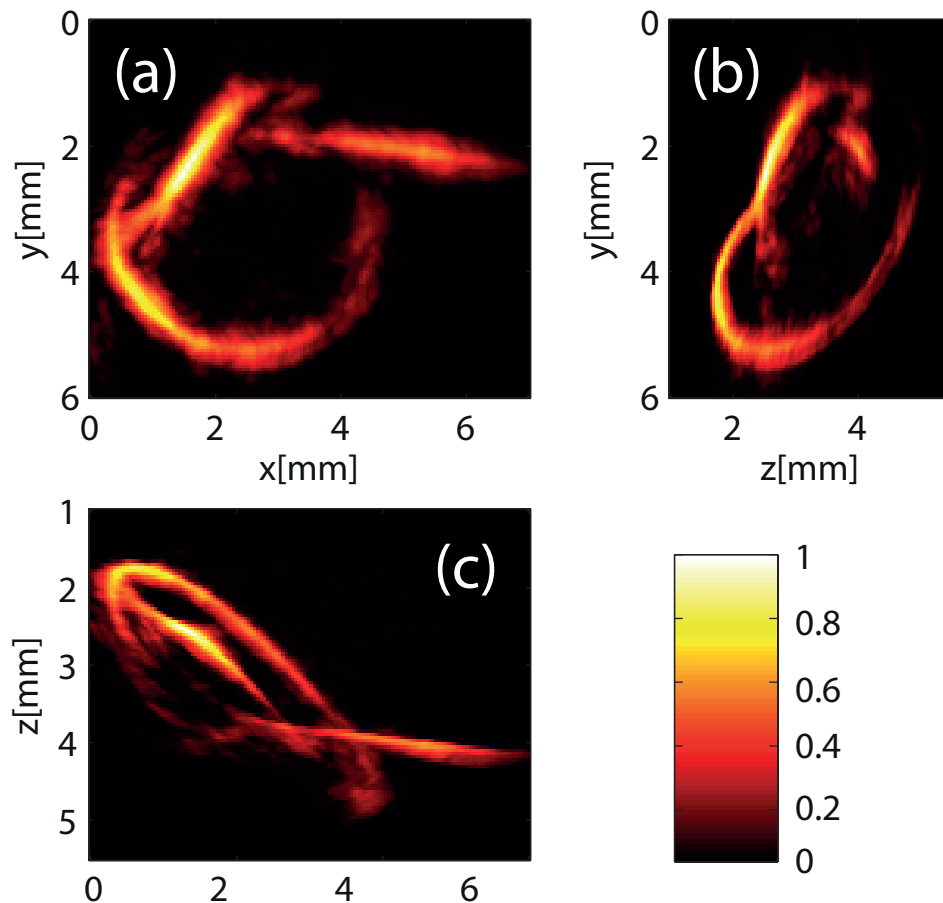


**Figure 9.** RECONSTRUCTION RESULTS USING COMPRESSED SENSING MEASUREMENTS. Maximum intensity projections of a silicone loop along the  $z$ -direction (a), the  $x$ -direction (b), and the  $y$ -direction (c).

Using this setup, point-wise pressure data on the measurement surface have been collected for  $4331 = 71 \times 61$  detector positions on over an area of  $7 \text{ mm} \times 6 \text{ mm}$ . From this data we generated  $m = 1116$  compressed sensing measurements, where

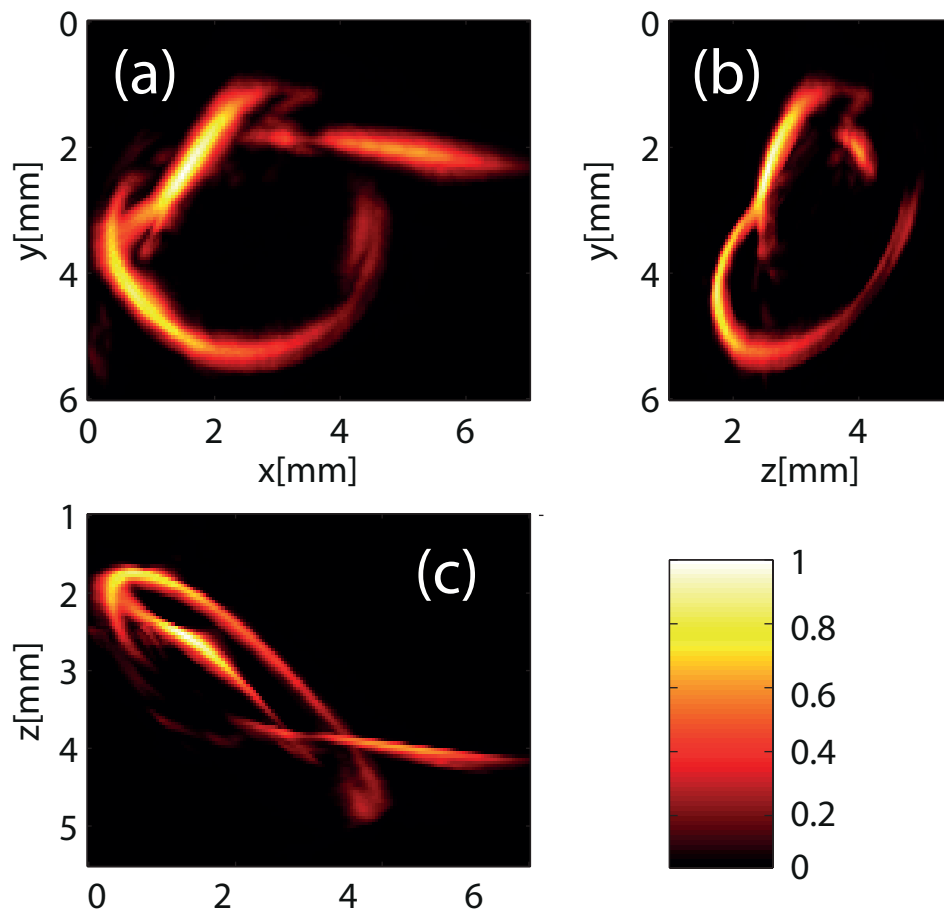


**Figure 10.** RECONSTRUCTION RESULTS USING FULL MEASUREMENTS. Maximum intensity projections of a silicone loop along the  $z$ -direction (a), the  $x$ -direction (b), and the  $y$ -direction (c).

each detector location has been used  $d = 10$  times in total. Figure 9 shows the maximum amplitude projections along the  $z$ ,  $x$ , and  $y$ -direction, respectively, of the three-dimensional reconstruction from compressed sensing data using Algorithm 3. The sparsified pressure has been reconstructed by minimizing (10) with the FISTA using 500 iterations and a regularization parameter of  $10^{-5}$ . Further, the three-dimensional reconstruction has been evaluated at  $110 \times 122 \times 142$  equidistant grid points. For comparison purpose, in Figure 10 we show the maximum amplitude projections from the UBP Algorithm 1 applied to the original data set. We observe that there is only a small difference between the reconstructions in terms of quality measures such as contrast, resolution and signal to noise ratio. Only, the structures in the compressed sensing reconstruction appear to be slightly less regular. A detailed quality evaluation is beyond the scope of this paper, which aims at serving as proof of principle of our two-stage compressed sensing approach with sparsifying transform. However the compressed sensing approach uses only a fourth of the number of measurements of the original data set. This clearly demonstrates the potential of our compressed sensing scheme for decreasing the number of measurements while keeping the image quality.



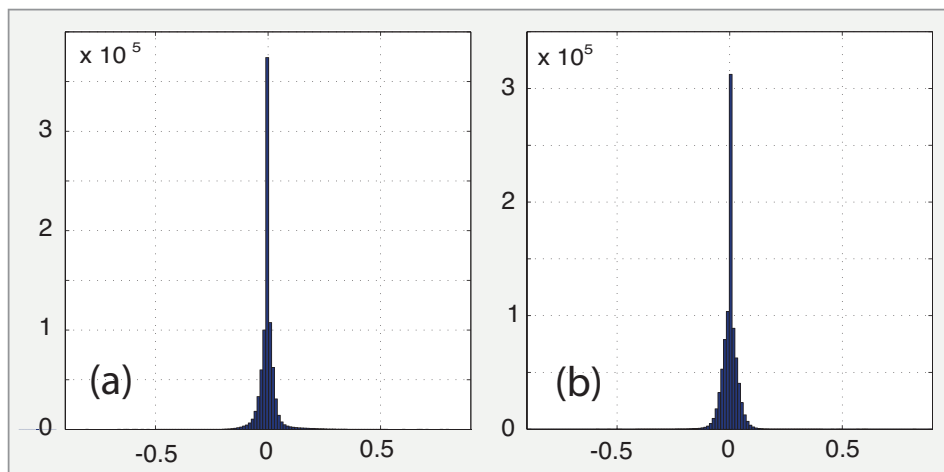


**Figure 11.** HISTOGRAMS OF EXPERIMENTAL DATA. (a) Histogram for measured pressure values (normalized to the interval  $[0, 1]$ ). (b) The same after applying the sparsifying transform  $\mathbf{T}$ .

Figure 11 shows histograms of the pressure values before and after applying the sparsifying temporal transform. In both cases the histograms are concentrated around the value zero. This implies the approximate sparsity and therefore justifies our approach, even if the phantom is not a superposition of uniformly absorbing spheres. It further shows that for the present situation one could even apply our two-stage procedure without applying the sparsifying transform.

#### 4. Discussion

To ensure sparsity in PAT, the standard approach is choosing a suitable basis which sparsely represents the pressure data on the measurement surface. In this paper we developed a different concept based on sparsifying temporal transforms. Since any temporal transform intertwines with the spatial measurements our approach can be used in combination with any measurement matrix that is incoherent to the pixel basis. This includes binary random matrices such as Bernoulli, Hadamard, or expander matrices (see Appendix A for details). According to the compressed sensing theory, expander matrices can be used with binary entries 0 and 1. Bernoulli and Hadamard matrices, on the other hand, should be used with zero mean (achieved, for example taking  $\pm 1$  as binary entries). As 0/1 entries can be practically most simple be realized, for Bernoulli and Hadamard matrices the mean value has to be subtracted after the measurements process [9]. Avoiding such additional data manipulations is one reason why we currently work with expander matrices. Another reason is the sparse structure of expander matrices which can be used to accelerate image reconstruction. In future work we will also investigate the use of Bernoulli and Hadamard in combination with sparsifying temporal or spatial transforms, and compare the performance of these measurement ensembles in different situations.

As mentioned in the introduction, patterned interrogation can be used to practically implement compressed sensing in PAT. It has been realized by using a digital micromirror device [9, 10], where a Fabry-Perot sensor was illuminated by a wide-field collimated beam. The reflected beam, carrying the ultrasonic information on the acoustic field, was then sampled by the DMD and the spatially integrated response was measured by a photodiode. Another possibility is the application of spatial light modulators (SLMs), which are able to modulate the phase of the light. By using such SLMs arbitrary interrogation patterns can be generated directly on a sample surface [33]. SLMs are commercially available for a wavelength of 1550 nm, which is the most common wavelength used in optical detection schemes. However, also for other wavelengths appropriate devices are available. State-of-the-art SLMs provide typical resolutions between  $1920 \times 1080$  pixels and  $4094 \times 2464$  pixels, which is sufficient for the compressed imaging scheme presented in this work. For a resolution of  $1920 \times 1080$ , the typically achieved frame rate is 60 Hz. This is faster than the pulse repetition rate of commonly used excitation laser sources for PAT, thus enabling single shot measurements. If a faster repetition rate is required, one could use SLMs with a higher frame rate. These, however, usually exhibit lower resolution.

For the Fabry-Perot etalon sensors, the wavelength of the interrogation beam has to be tuned, such that it corresponds to the maximum slope of the transfer function of the sensor. Since for the patterned interrogation scheme only one wavelength is used for the acquisition of the integrated response this demands high quality Fabry-Perot sensors with highly uniform sensor properties. For non-contact schemes, using Mach-Zehnder or Michelson based demodulation, the sensitivity does not depend on the wavelength as the sensor is stabilized by the relative phase between the interrogation beam and a reference beam. However, if the surface is not adequately flat, the phase of the reflected light is spatially varying. Thereby, the sensitivity changes over the detection surface, and even locations with zero or low response could exist. Here, the phase modulation capability of SLMs offers the possibility to compensate for this. In general, each pixel of a SLM can shift the phase of light at least up to  $2\pi$  and the resulting phase distribution is impressed on the reflected beam. Separate lens functions can be applied to each detection point individually by using distinct kernels for each of these points [34]. In case the shape of the sample surface is known, the phase at each detection point can be chosen to compensate for the phase shifts caused by the imperfect sample surface. With this method it is even possible to choose different focal distances for each detection point, so that detection on even rougher surfaces could be facilitated.

## 5. Conclusion

To speed up the data collection process in sequential scanning PAT while keeping sensitivity high without significantly increase the production costs, one has to reduce the number of spatial measurements. In this paper we proposed a compressed sensing scheme for that purpose using random measurements in combination with a sparsifying

temporal transform. We presented a selected review of compressed sensing that demonstrates the role of sparsity and randomness for high resolution recovery. Using general results from compressed sensing we were able to derive theoretical recovery guarantees for our approach based on sparsifying temporal transforms. Further, this comes with a fast algorithmic implementation.

## Acknowledgments

This work has been supported by the Austrian Science Fund (FWF), project number P25584-N20, the Christian Doppler Research Association (Christian Doppler Laboratory for Photoacoustic Imaging and Laser Ultrasonics), the European Regional Development Fund (EFRE) in the framework of the EU-program Regio 13, the federal state Upper Austria. S. Moon thanks University of Innsbruck for its hospitality during his visit. The work of S. Moon has been supported by the National Research Foundation of Korea grant funded by the Korea government (MSIP) (2015R1C1A1A01051674) and the TJ Park Science Fellowship of POSCO TJ Park Foundation.

## Appendix A. Ingredients from compressed sensing

In this section we present the basic ingredients of compressed sensing that explains the choice of the measurement matrices and the role of sparsity in PAT. The aim of compressed sensing is to stably recover a signal or image modeled by vector  $\mathbf{x} \in \mathbb{R}^n$  from measurements

$$\mathbf{y} = \mathbf{A}\mathbf{x} + \mathbf{e}. \quad (\text{A.1})$$

Here  $\mathbf{A} \in \mathbb{R}^{m \times n}$  with  $m \ll n$  is the measurement matrix,  $\mathbf{e}$  is an unknown error (noise) and  $\mathbf{y}$  models the given noisy data. The basic components that make compressed sensing possible are sparsity (or compressibility) of the signal  $\mathbf{x}$  and some form of randomness in the measurement matrix  $\mathbf{A}$ .

### Appendix A.1. Sparsity and compressibility

The first basic ingredient of compressed sensing is sparsity, that is defined as follows.

**Definition 1** (Sparse signals).

Let  $s \in \mathbb{N}$  and  $\mathbf{x} \in \mathbb{R}^n$ . The vector  $\mathbf{x}$  is called  $s$ -sparse, if  $\|\mathbf{x}\|_0 := \#\{i \in \{1, \dots, n\} \mid \mathbf{x}[i] \neq 0\} \leq s$ . One informally calls  $\mathbf{x}$  sparse, if it is  $s$ -sparse for sufficiently small  $s$ .

In Definition 1,  $\#(S)$  stands for the number of elements in a set  $S$ . Therefore  $\|\mathbf{x}\|_0$  counts the number of non-zero entries in the vector  $\mathbf{x}$ . In the mathematical sense  $\|\cdot\|_0$  is neither a norm or a quasi-norm<sup>§</sup> but it is common to call  $\|\cdot\|_0$  the  $\ell^0$ -norm. It

<sup>§</sup> A quasi-norm satisfies all axioms of a norm, except that the triangle inequality is replaced by the weaker inequality  $\|\mathbf{x}_1 + \mathbf{x}_2\| \leq K(\|\mathbf{x}_1\| + \|\mathbf{x}_2\|)$  for some constant  $K \geq 1$ .

satisfies  $\|x\|_0 = \lim_{p \downarrow 0} \|\mathbf{x}\|_p^p$ , where

$$\|\mathbf{x}\|_p := \sqrt[p]{\sum_{i=1}^n |\mathbf{x}[i]|^p} \quad \text{with } p > 0, \quad (\text{A.2})$$

stands for the  $\ell^p$ -norm. Recall that  $\|\cdot\|_p$  is indeed a norm for  $p \geq 1$  and a quasi-norm for  $p \in (0, 1)$ .

Signals of practical interest are often not sparse in the strict sense, but can be well approximated by sparse vectors. For that purpose we next define the  $s$ -term approximation error that can be used as a measure for compressibility.

**Definition 2** (Best  $s$ -term approximation error).

Let  $s \in \mathbb{N}$  and  $\mathbf{x} \in \mathbb{R}^n$ . One calls

$$\sigma_s(\mathbf{x}) := \inf\{\|\mathbf{x} - \mathbf{x}_s\|_1 \mid \mathbf{x}_s \in \mathbb{R}^n \text{ is } s\text{-sparse}\}$$

the best  $s$ -term approximation error of  $\mathbf{x}$  (with respect to the  $\ell^1$ -norm).

The best  $s$ -term approximation error  $\sigma_s(\mathbf{x})$  measures, in terms of the  $\ell^1$ -norm, how much the vector  $\mathbf{x}$  fails to be  $s$ -sparse. One calls  $\mathbf{x} \in \mathbb{R}^n$  compressible, if  $\sigma_s(\mathbf{x})$  decays sufficiently fast with increasing  $s$ . The estimate (see [35])

$$\sigma_s(\mathbf{x}) \leq \frac{q(1-q)^{1/q-1}}{s^{1/q-1}} \|\mathbf{x}\|_q \quad \text{for } q \in (0, 1) \quad (\text{A.3})$$

shows that a signal is compressible if its  $\ell^q$ -norm is sufficiently small for some  $q < 1$ .

### Appendix A.2. The RIP in compressed sensing

Stable and robust recovery of sparse vectors requires the measurement matrix to well separate sparse vectors. The RIP guarantees such a separation.

**Definition 3** (Restricted isometry property (RIP)).

Let  $s \in \mathbb{N}$  and  $\delta \in (0, 1)$ . The measurement matrix  $\mathbf{A} \in \mathbb{R}^{m \times n}$  is said to satisfy the RIP of order  $s$  with constant  $\delta$ , if, for all  $s$ -sparse  $\mathbf{x} \in \mathbb{R}^n$ ,

$$(1 - \delta)\|\mathbf{x}\|_2^2 \leq \|\mathbf{A}\mathbf{x}\|_2^2 \leq (1 + \delta)\|\mathbf{x}\|_2^2. \quad (\text{A.4})$$

We write  $\delta_s$  for the smallest constant satisfying (A.4).

In the recent years, many sparse recovery results have been derived under various forms of the RIP. Below we give a result derived recently in [36].

**Theorem 4** (Sparse recovery under the RIP).

Let  $\mathbf{x} \in \mathbb{R}^n$  and let  $\mathbf{y} \in \mathbb{R}^m$  satisfy  $\|\mathbf{y} - \mathbf{A}\mathbf{x}\|_2 \leq \epsilon$  for some noise level  $\epsilon > 0$ . Suppose that  $\mathbf{A} \in \mathbb{R}^{m \times n}$  satisfies the RIP of order  $2s$  with constant  $\delta_{2s} < 1/2$ , and let  $\mathbf{x}_\star$  solve

$$\begin{aligned} & \text{minimize}_{\mathbf{z}} \|\mathbf{z}\|_1 \\ & \text{such that } \|\mathbf{A}\mathbf{z} - \mathbf{y}\|_2 \leq \epsilon. \end{aligned} \quad (\text{A.5})$$

Then, for constants  $c_1, c_2$  only depending on  $\delta_{2s}$ ,  $\|\mathbf{x} - \mathbf{x}_\star\|_2 \leq c_1 \sigma_s(\mathbf{x})/\sqrt{s} + c_2 \epsilon$ .

*Proof.* See [36].  $\square$

Theorem 4 states stably and robust recovery for measurement matrices satisfying the RIP. The error estimate consists of two terms:  $c_2\epsilon$  is due to the data noise and is proportional to the noise level (stability with respect to noise). The term  $c_1\sigma_s(\mathbf{x})/\sqrt{s}$  accounts for the fact that the unknown may not be strictly  $s$ -sparse and shows robustness with respect to the model assumption of sparsity.

No deterministic construction is known providing large measurement matrices satisfying the RIP. However, several types of random matrices are known to satisfy the RIP with high probability. Therefore, for such measurement matrices, Theorem 4 yields stable and robust recovery using (A.5). We give two important examples of binary random matrices satisfying the RIP [35].

**Example 5** (Bernoulli matrices).

A binary random matrix  $\mathbf{B}_{m,n} \in \{-1, 1\}^{m \times n}$  is called Bernoulli matrix if its entries are independent and take the values  $-1$  and  $1$  with equal probability. A Bernoulli matrix satisfies  $\delta_{2s} < \delta$  with probability tending to 1 as  $m \rightarrow \infty$ , if

$$m \geq C_\delta s (\log(n/s) + 1) \quad (\text{A.6})$$

for some constant  $C_\delta > 0$ . Consequently, Bernoulli-measurements yield stable and robust recovery by (A.5) provided that (A.6) is satisfied.

Bernoulli matrices are dense and unstructured. If  $n$  is large then storing and applying such a matrix is expensive. The next example gives a structured binary matrix satisfying the RIP.

**Example 6** (Subsampled Hadamard matrices).

Let  $n$  be a power of two. The Hadamard matrix  $\mathbf{H}_n$  is a binary orthogonal and self-adjoint  $n \times n$  matrix that takes values in  $\{-1, 1\}$ . It can be defined inductively by  $\mathbf{H}_1 = 1$  and

$$\mathbf{H}_{2n} := \frac{1}{\sqrt{2}} \begin{bmatrix} \mathbf{H}_n & \mathbf{H}_n \\ \mathbf{H}_n & -\mathbf{H}_n \end{bmatrix}. \quad (\text{A.7})$$

Equation (A.7) also serves as the basis for evaluating  $\mathbf{H}_n \mathbf{x}$  with  $n \log n$  floating point operations. A randomly subsampled Hadamard matrix has the form  $\mathbf{P}_{m,n} \mathbf{H}_n \in \{-1, 1\}^{m \times n}$ , where  $\mathbf{P}_{m,n}$  is a subsampling operator that selects  $m$  rows uniformly at random. It satisfies  $\delta_{2s} < \delta$  with probability tending to 1 as  $n \rightarrow \infty$ , if

$$m \geq D_\delta s \log(n)^4 \quad (\text{A.8})$$

for some constant  $D_\delta > 0$ . Consequently, randomly subsampled Hadamard matrices again yield stable and robust recovery using (A.5).

### Appendix A.3. Compressed sensing using lossless expanders

A particularly useful type of binary measurement matrices for compressed sensing are sparse matrices having exactly  $d$  ones in each column. Such a measurement matrix can be interpreted as the adjacency matrix of a left  $d$ -regular bipartite graph.

Consider the bipartite graph  $(L, R, E)$  where  $L := \{1, \dots, n\}$  is the set of left vertices,  $R := \{1, \dots, m\}$  the set of right vertices and  $E \subseteq L \times R$  the set of edges. Any element  $(i, j) \in E$  can be interpreted as a edge joining vertices  $i$  and  $j$ . We write

$$N(I) := \{j \in R \mid \exists i \in I \text{ with } (i, j) \in E\}$$

for the set of (right) neighbors of  $I \subseteq L$ .

**Definition 7** (Left  $d$ -regular graph).

The bipartite graph  $(L, R, E)$  is called  $d$ -left regular, if  $\sharp[N(\{i\})] = d$  for every  $i \in L$ .

According to Definition 7,  $(L, R, E)$  is left  $d$ -regular if any left vertex is connected to exactly  $d$  right vertices. Recall that the adjacency matrix  $\mathbf{A} \in \{0, 1\}^{m \times n}$  of  $(L, R, E)$  is defined by  $\mathbf{A}[j, i] = 1$  if  $(i, j) \in E$  and  $\mathbf{A}[j, i] = 0$  if  $(i, j) \notin E$ . Consequently the adjacency matrix of a  $d$ -regular graph contains exactly  $d$  ones in each column. If  $d$  is small, then the adjacency matrix of a left  $d$ -regular bipartite graph is sparse.

**Definition 8** (Lossless expander).

Let  $s \in \mathbb{N}$  and  $\theta \in (0, 1)$ . A  $d$ -left regular graph  $(L, R, E)$  is called an  $(s, d, \theta)$ -lossless expander, if

$$\sharp[N(I)] \geq (1 - \theta) d \sharp[I] \text{ for } I \subseteq L \text{ with } \sharp[I] \leq s. \quad (\text{A.9})$$

We write  $\theta_s$  for the smallest constant satisfying (A.9).

It is clear that the adjacency matrix of a  $d$ -regular graph satisfies  $\sharp[N(I)] \leq d \sharp[I]$ . Hence an expander graph satisfies the two sided estimate  $(1 - \theta) d \sharp[I] \leq \sharp[N(I)] \leq d \sharp[I]$ . Opposed to Bernoulli and subsampled Hadamard matrices, a lossless expander does not satisfy the  $\ell^2$ -based RIP. However, in such a situation, one can use the following alternative recovery result.

**Theorem 9** (Sparse recovery for lossless expander).

Let  $\mathbf{x} \in \mathbb{R}^n$  and let  $\mathbf{y} \in \mathbb{R}^m$  satisfy  $\|\mathbf{y} - \mathbf{Ax}\|_1 \leq \epsilon$  for some noise level  $\epsilon > 0$ . Suppose that  $\mathbf{A}$  is the adjacency matrix of a  $(2s, d, \theta_{2s})$ -lossless expander having  $\theta_{2s} < 1/6$  and let  $\mathbf{x}_*$  solve

$$\begin{aligned} & \text{minimize}_{\mathbf{z}} \|\mathbf{z}\|_1 \\ & \text{such that } \|\mathbf{Az} - \mathbf{y}\|_1 \leq \epsilon. \end{aligned} \quad (\text{A.10})$$

Then, for constants  $c_1, c_2$  only depending on  $\theta_{2s}$ , we have  $\|\mathbf{x} - \mathbf{x}_*\|_1 \leq c_1 \sigma_s(\mathbf{x}) + c_2 \epsilon / d$ .

*Proof.* See [37, 35]. □

Choosing a  $d$ -regular bipartite graph uniformly at random yields a lossless expander with high probability. Therefore, Theorem 9 yields stable and robust recovery for such type of random matrices.

**Example 10** (Expander matrix).

Take  $\mathbf{A} \in \{0, 1\}^{m \times n}$  as the adjacency matrix of a randomly chosen left  $d$ -regular bipartite graph. Then  $\mathbf{A}$  has exactly  $d$  ones in each column, whose locations are uniformly distributed. Suppose further that for some constant  $c_\theta$  only depending on  $\theta$  the parameters  $d$  and  $m$  have been selected according to

$$m \geq c_\theta s(\log(n/s) + 1)$$

$$d = \left\lceil \frac{2 \log(n/s) + 2}{\theta} \right\rceil.$$

Then,  $\theta_s \leq \theta$  with probability tending to 1 as  $n \rightarrow \infty$ . Consequently, for the adjacency matrix of a randomly chosen left  $d$ -regular bipartite graphs, called expander matrix, we have stable and robust recovery by (A.10).

**References**

- [1] P. Beard. Biomedical photoacoustic imaging. *Interface focus*, 1(4):602–631, 2011.
- [2] L. V. Wang. Multiscale photoacoustic microscopy and computed tomography. *Nature Phot.*, 3(9):503–509, 2009.
- [3] M. Xu and L. V. Wang. Photoacoustic imaging in biomedicine. *Rev. Sci. Instruments*, 77(4):041101 (22pp), 2006.
- [4] E. Zhang, J. Laufer, and P. Beard. Backward-mode multiwavelength photoacoustic scanner using a planar fabry-perot polymer film ultrasound sensor for high-resolution three-dimensional imaging of biological tissues. *Appl. Opt.*, 47(4):561–577, 2008.
- [5] T. Berer, A. Hochreiner, S. Zamiri, and P. Burgholzer. Remote photoacoustic imaging on solid material using a two-wave mixing interferometer. *Opt. Lett.*, 35(24):4151–4153, 2010.
- [6] T. Berer, A. Leiss-Holzinger, E. Hochreiner, J. Bauer-Marschallinger, and A. Buchsbaum. Multimodal non-contact photoacoustic and optical coherence tomography imaging using wavelength-division multiplexing. *J. Biomed. Opt.*, 20(4):046013, 2015.
- [7] J. Eom, S. Park, and B. B. Lee. Noncontact photoacoustic tomography of in vivo chicken chorioallantoic membrane based on all-fiber heterodyne interferometry. *J. Biomed. Opt.*, 20(4):106007, 2015.
- [8] N. Huynh, O. Ogunlade, E. Zhang, B. Cox, and P. Beard. Photoacoustic imaging using an 8-beam fabry-perot scanner. *Proc. SPIE*, 9708:97082L, 2016.
- [9] N. Huynh, E. Zhang, M. Betcke, S. Arridge, P. Beard, and B. Cox. Patterned interrogation scheme for compressed sensing photoacoustic imaging using a fabry perot planar sensor. *Proc. SPIE*, 8943:894327–5, 2014.
- [10] N. Huynh, E. Zhang, M. Betcke, S. Arridge, P. Beard, and B. Cox. Single-pixel optical camera for video rate ultrasonic imaging. *Optica*, 3(1):26–29, 2016.
- [11] M. Sandbichler, F. Kraemer, T. Berer, P. Burgholzer, and M. Haltmeier. A novel compressed sensing scheme for photoacoustic tomography. *SIAM J. Appl. Math.*, 75(6):2475–2494, 2015.
- [12] P. Burgholzer, M. Sandbichler, F. Kraemer, T. Berer, and M. Haltmeier. Sparsifying transformations of photoacoustic signals enabling compressed sensing algorithms. *Proc. SPIE*, 9708:970828–8, 2016.
- [13] E. J. Candès, J. Romberg, and T. Tao. Robust uncertainty principles: exact signal reconstruction from highly incomplete frequency information. *IEEE Trans. Inf. Theory*, 52(2):489–509, 2006.
- [14] E. J. Candès and T. Tao. Near-optimal signal recovery from random projections: universal encoding strategies? *IEEE Trans. Inf. Theory*, 52(12), 2006.
- [15] D. L. Donoho. Compressed sensing. *IEEE Trans. Inf. Theory*, 52(4):1289–1306, 2006.

- [16] E. Candès, L. Demanet, D. Donoho, and L. Ying. Fast discrete curvelet transforms. *Multiscale Model. Sim.*, 5:861–899, 2006.
- [17] S. Mallat. *A wavelet tour of signal processing: The sparse way*. Elsevier/Academic Press, Amsterdam, third edition, 2009.
- [18] A. Hochreiner, J. Bauer-Marschallinger, B. Burgholzer, P. Jakoby, and T. Berer. Non-contact photoacoustic imaging using a fiber based interferometer with optical amplification. *Biomed. Opt. Express*, 4(11):2322–2331, 2013.
- [19] M. Xu and L. V. Wang. Universal back-projection algorithm for photoacoustic computed tomography. *Phys. Rev. E*, 71(1):016706, 2005.
- [20] P. Burgholzer, J. Bauer-Marschallinger, H. Grün, M. Haltmeier, and G. Paltauf. Temporal back-projection algorithms for photoacoustic tomography with integrating line detectors. *Inverse Probl.*, 23(6):S65–S80, 2007.
- [21] M. Haltmeier. Inversion of circular means and the wave equation on convex planar domains. *Comput. Math. Appl.*, 65(7):1025–1036, 2013.
- [22] F. Natterer. Photo-acoustic inversion in convex domains. *Inverse Probl. Imaging*, 6(2):315–320, 2012.
- [23] L. A. Kunyansky. Explicit inversion formulae for the spherical mean Radon transform. *Inverse Probl.*, 23(1):373–383, 2007.
- [24] M. Haltmeier. Universal inversion formulas for recovering a function from spherical means. *SIAM J. Math. Anal.*, 46(1):214–232, 2014.
- [25] M. Haltmeier and S. Pereverzyev, Jr. The universal back-projection formula for spherical means and the wave equation on certain quadric hypersurfaces. *J. Math. Anal. Appl.*, 429(1):366–382, 2015.
- [26] M. Grasmair, M. Haltmeier, and O. Scherzer. Sparse regularization with  $l^q$  penalty term. *Inverse Probl.*, 24(5):055020, 13, 2008.
- [27] M. Haltmeier. Stable signal reconstruction via  $\ell^1$ -minimization in redundant, non-tight frames. *IEEE Trans. Signal Process.*, 61(2):420–426, 2013.
- [28] J. Provost and F. Lesage. The application of compressed sensing for photo-acoustic tomography. *IEEE Trans. Med. Imag.*, 28(4):585–594, 2009.
- [29] Z. Guo, C. Li, L. Song, and L. V. Wang. Compressed sensing in photoacoustic tomography in vivo. *J. Biomed. Opt.*, 15(2):021311–021311, 2010.
- [30] J. Meng, L. V. Wang, D. Liang, and L. Song. In vivo optical-resolution photoacoustic computed tomography with compressed sensing. *Optics letters*, 37(22):4573–4575, 2012.
- [31] G. J. Diebold, T. Sun, and M. I. Khan. Photoacoustic monopole radiation in one, two, and three dimensions. *Phys. Rev. Lett.*, 67:3384–3387, Dec 1991.
- [32] A. Beck and M. Teboulle. A fast iterative shrinkage-thresholding algorithm for linear inverse problems. *SIAM J. Imaging Sci.*, 2(1):183–202, 2009.
- [33] C. Grünsteidl, I. A. Veres, J. Roither, P. Burgholzer, T. W. Murray, and T. Berer. Spatial and temporal frequency domain laser-ultrasound applied in the direct measurement of dispersion relations of surface acoustic waves. *Applied Physics Letters*, 102(1):011103, 2013.
- [34] Jennifer E. Curtis, Brian A. Koss, and David G. Grier. Dynamic holographic optical tweezers. *Optics Communications*, 207(1–6):169–175, 2002.
- [35] S. Foucart and H. Rauhut. *A mathematical introduction to compressive sensing*. Springer, 2013.
- [36] T. T. Cai and A. Zhang. Sharp RIP bound for sparse signal and low-rank matrix recovery. *Appl. Comput. Harmon. Anal.*, 35(1):74–93, 2013.
- [37] R. Berinde, A. C. Gilbert, P. Indyk, H. Karloff, and M. J. Strauss. Combining geometry and combinatorics: A unified approach to sparse signal recovery. In *46th Annual Allerton Conference on Communication, Control, and Computing, 2008*, pages 798–805, 2008.